

GT2011-45*) (

PASSIVE TRACER VALIDITY FOR COOLING EFFECTIVENESS THROUGH FLOW COMPUTATION IN A TURBINE RIM SEAL ENVIRONMENT

Guillaume Boutet-Blais, Julie Lefrancois, Guy Dumas,
Steve Julien, Jean-Francois Harvey
Laboratoire de Mecanique des Fluides Numerique
Department of Mechanical Engineering
Laval University
Quebec City, Quebec, G1V 0A6
Canada
Email: gdumas@gmc.ulaval.ca

Remo Marini, Jean-Francois Caron
Pratt & Whitney Canada
1000 Marie-Victorin
Longueuil, Quebec, J4G 1A1
Canada

ABSTRACT

This paper reports the first phase of an investigation aiming to determine the validity of using a CO₂ marker in cold rig experiments to characterize the thermal performances of turbine rim seals under actual engine operating conditions. For comparison purposes, simulations are carried out for two sets of operating conditions, namely cold rig (with uniform low temperature) and real turbine thermal conditions (high temperature gaspath and cold purge flow). Sealing effectiveness based on the CO₂ diagnostic under cold rig operating conditions is compared to sealing effectiveness based on the computed temperature field under real engine temperature conditions. Unsteady RANS simulations with different purge flow rates are performed. Tested geometries include a 180° domain presenting a simplified rim seal geometry with no vanes nor blades in the gaspath, and a 24° sector of a complete turbine stage including 3 vanes and 4 blades. Three-dimensional flow structures known to affect ingestion are found with both geometries but appear to be sensitive to the differences in operating conditions. Indeed, their circumferential number and strength differ between the two scenarios of conditions. Furthermore, it is found that the cold rig predictor tends to slightly overestimate the sealing effectiveness, while providing nonetheless the right trends and reasonably accurate average values in levels of actual sealing. At this stage of the investigation, we conclude that it seems adequate to use a passive tracer in cold rig experiments to compare performances of rim seal designs.

NOMENCLATURE

ILT	isothermal low temperature rig conditions,
RET	real engine temperature conditions,
C_w	viscous non-dimensional purge flow rate $\dot{m}_{\text{purge}} / \mu_{\text{purge}} r_{\text{hub}}$,
C_x	axial velocity at the vane trailing edge,
D_ψ	turbulent mass diffusivity,
P	static pressure,
P_0	total pressure at gaspath inlet,
T	static temperature,
T_{gaspath}	static temperature at gaspath inlet,
T_{purge}	static temperature at purge flow inlet,
U_{hub}	hub velocity at the vane trailing edge, $r_0 \Omega$,
\dot{m}_{gaspath}	mass flow rate at the gaspath entrance of the computational domain,
\dot{m}_{outlet}	mass flow rate imposed at the exit of the computational domain,
\dot{m}_{purge}	mass flow rate imposed at the purge flow entrance of the computational domain,
r_0	radius of the gaspath hub at the vane trailing edge,
x, r, θ	cylindrical coordinates,
Re_ϕ	Rotational Reynolds number, $\Omega r_0 / \nu_{\text{gaspath}}$,
Ω	rotor angular velocity,
Φ_{purge}	non-dimensional purge flow rate, $\dot{m}_{\text{purge}} / \dot{m}_{\text{gaspath}}$,

η	sealing effectiveness (1 corresponds to perfect seal),
η_{CO_2}	sealing effectiveness based on CO_2 prediction, $(\psi - \psi_{\text{gaspath}})/(\psi_{\text{purge}} - \psi_{\text{gaspath}})$,
η_{thermal}	sealing effectiveness based on temperature, $(T_{\text{gaspath}} - T)/(T_{\text{gaspath}} - T_{\text{purge}})$,
ψ	CO_2 concentration per unit mass.

1 INTRODUCTION

Appropriate and well-designed cooling and sealing have become major issues in modern engine and gas turbine manufacturing. It is imperative to minimize the ingestion of hot gas from the main gaspath flow through the rim seal and into the rotor-stator cavity in order to preserve the integrity of the turbine's disk. Experimental studies of disk cooling are generally performed in a rig operating at ambient temperature using a passive CO_2 tracer to evaluate ingestion from the main gaspath, a procedure also used in many numerical investigations. The use of the passive tracer in a cold temperature environment discards the need for more expensive rig setups involving higher temperatures and pressures. Temperature differences between purge and gaspath inlets are transposed as inlet gas concentration differences and thermodynamic effects are neglected. To the authors' knowledge, the validity of using CO_2 to establish sealing effectiveness of turbine rim seal designs destined to operate under real engine conditions has never been investigated thoroughly. This work is a first step towards that goal.

This paper intends to assess, through numerical simulations, the validity of using a CO_2 passive tracer in a cold rig to verify the actual sealing effectiveness of a design. This study is a first step towards a complete assessment of the passive tracer usage as it is restricted here to subsonic flow conditions, and it does not take into account heat transport through wall conduction. This project is carried out at Laval University and is part of an international CRIAQ¹ project with the collaboration of Pratt and Whitney Canada. The global objective of this larger research program is to provide better ingress diagnoses while improving our understanding of the whole ingestion process, especially regarding the detailed flow physics of disk cavities and flow structures that may develop in the rim cavity region. In the present paper, URANS simulations of turbine rim seals are performed to investigate the representativity of the tracer field under cold rig operating conditions with respect to the predicted temperature field under real engine thermal conditions. The present calculations are based on a rig geometry used by experimental partners.

In the last few decades, turbine rim seal research has much focused on the different factors causing ingestion. Early works by Owen and Rogers [1], Phadke and Owen [2, 3], Chew *et al.* [4, 5], and Bayley and Childs [6] have paved the way describing the physics surrounding the ingestion phenomenon. From these studies, it is known that rim and cavity geometries, disk-pumping mechanisms, overall operating conditions and vane-blade interactions are the main factors driving ingress in a turbine rim seal environment. It is now well accepted that steady-state simulations underestimate the level of ingress within the cavity. As reported by Hills *et al.* [7], Gentilhomme *et al.* [8], Roy *et al.* [9] and Chew [10], turbulent, three dimensional and unsteady effects have to be properly taken into account to correctly model the flow dynamics in a rim seal environment. In more recent numerical and experimental studies, namely by Julien *et al.* [11], Jakoby *et al.* [12], Cao *et al.* [13] and Boudet *et al.* [14], the existence of large-scale structures has been reported and their pressure traces have been correlated to ingress paths. As shown in [11], these structures are not necessarily related to the vane or the blade counts and they can account for an important part of the ingestion phenomenon. Relative effects of these structures on the CO_2 and temperature fields have never been investigated. Using a large size sector in the circumferential direction has thus been shown to be necessary to properly capture the flow patterns in the cavity.

The commercial code *ANSYS CFX* [15] is used in this work to perform 3-D unsteady RANS simulations. Low purge flow rate conditions, associated with complex three-dimensional flow structures and significant ingress from the main gaspath, are set for an empty gaspath configuration as well as on a large periodic sector of a complete turbine stage with vanes and blades. Two main types of flow boundary conditions are tested for each geometry. Typical rig conditions are used for the Isothermal Low Temperature-low pressure reference case (referred to as *ILT*). From these, high temperature-high pressure conditions corresponding to typical Real Engine Temperature environment in subsonic regime (referred to as *RET*) are derived from standard turbomachinery parameters “ Ω/\sqrt{T} ” and “ $\dot{m}_{\text{gaspath}}\sqrt{T}/P_{\text{gaspath}}$ ” (for similar geometries and gases) thus preserving the same velocity triangles between the two scenarios.

Despite the differences arising in rotating speeds, gaspath pressures, temperatures, and mass flow rates between these two types of simulation conditions, the objective here is to demonstrate that, nonetheless, CO_2 concentration field in a rig environment and actual temperature field in a real engine are similar, and that sealing efficiency of a new design can be usefully asserted with a traditional cold rig experiment.

¹Consortium for Research and Innovation in Aerospace in Quebec

2 THEORETICAL BACKGROUND

Studies where CO_2 is used as a passive tracer are numerous in turbine rim seal research. This technique involves transport of the CO_2 concentration ψ which is governed, for the case of a turbulent flow, by a mass transport equation :

$$\frac{\partial(\rho \psi)}{\partial t} + \nabla \cdot (\rho \mathbf{U} \psi) = \nabla \cdot \left(\left(\rho D_{\psi} + \frac{\mu_t}{Sc_t} \right) \nabla \psi \right),$$

where ρ is the density of the main gas, ψ is the concentration per unit mass, D_{ψ} is the kinematic diffusivity of the CO_2 , Sc_t is the turbulent Schmidt number and μ_t is the dynamic turbulent viscosity. The expected analogy between the CO_2 concentration field and the thermal field rests on the similitude between their respective transport equation. Indeed, the thermal field is governed by the following Reynolds averaged energy equation :

$$\frac{\partial(\rho h_{tot})}{\partial t} - \frac{\partial p}{\partial t} + \nabla \cdot (\rho \mathbf{U} h_{tot}) = \nabla \cdot \left(\lambda \nabla T + \frac{\mu_t}{Pr_t} \nabla h \right) + V_w,$$

where $h_{tot} = h + \frac{1}{2}U^2 + \frac{1}{2}\overline{u^2}$, $h = c_p T$ with c_p being the heat capacity, Pr_t is the turbulent Prandtl number, λ is the thermal conductivity of the fluid and V_w represents the viscous work term, which was enabled in *CFX*. If viscous work is neglected (or negligible), the analogy between these two equations is valid if the flow is highly turbulent, that is when turbulent diffusion is considerably larger than molecular diffusion, and if the turbulent Prandtl number and the turbulent Schmidt number are almost equal. Default values of 0.9 for both Pr_t and Sc_t were used here.

Disk rotation causes viscous work through windage which acts as a source term, and is considered in this study. Another possible heat mechanism would be thermal conduction through material. This point, though it may be important, is not considered in this first study. In addition, it is important to point out that fluid properties may vary with temperature. Indeed, temperature would behave as a passive tracer only if the fluid properties among which density and viscosity are particularly critical, stay more or less homogeneous and constant. This happens when: 1) temperature differences are relatively small, and 2) compressibility effects are low. In the case of real engine operating temperatures, the first of these conditions is clearly not met since gaspath and purge flow temperatures differ significantly. In the present study, maximum values of 0.4 for Mach number are reached and the second condition is thus respected. However, in the case of higher rotating speeds and pressures, compressibility effects would be more important and the second condition may then be violated. This point will be investigated in a future step.

3 COMPUTATIONAL SETUP

Geometries

Two configurations are considered in this study. The first one (Configuration A) is a simple rotor-stator geometry without vanes nor blades with a single lip rim seal configuration. Figure 1 presents a $r-x$ view of this geometry. Stationary and rotating wall boundary conditions are used to account for the rotor-stator relative motion as viewed in a stationary reference frame. Overall dimensions are based on the experimental rig used for Configuration B. It covers an angular sector of 180° .

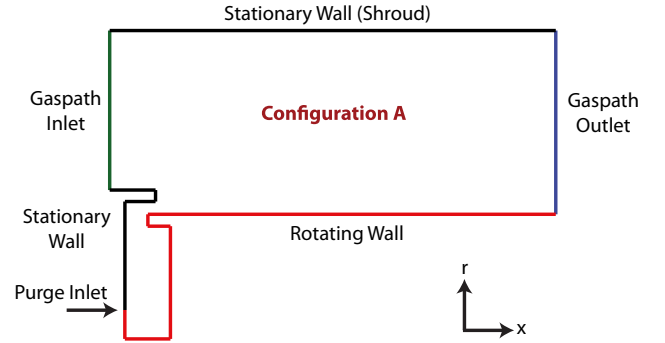


FIGURE 1. Configuration A : side view of the computational domain. Maximum and minimum radii are 0.3285 m and 0.2645 m respectively.

The second configuration (B) represents a complete turbine stage and disk cavity geometry of an experimental rig used by partners and earlier by Feiereisen *et al.* [16]. The actual rig has 44 inlet guide vanes and 58 rotor blades and operates at ambient temperature under low-Ma subsonic conditions. The rim seal is a double lip type. A $r-x$ view of the computational domain is shown in Fig. 2 and a 3-D view of the chosen sector is presented in Fig. 3. Calculation domain consists in two parts, a stationary domain containing stator vanes and the disk cavity while the turbine blades are part of the rotating domain. A non-conformal fluid-fluid interface located downstream of the cavity exit links both domains. The pitch correction algorithm provided by *ANSYS CFX* supports the choice of slightly different periodicities for both domains which allows the combination of a 3 vane (24.54°) and 4 blade (24.83°) sectors.

Numerical Setup

The commercial code *ANSYS CFX* 12.1 [15] is used in the present study. A conscious effort was made in order to reduce the number of mesh elements and thus limit computation times. First, preliminary computations with wall resolution ($y^+ \sim 1$, SST turbulence model) and wall modeling ($y^+ \sim 40$, $k-\epsilon$ model) showed minimal discrepancies and the latter ($k-\epsilon$ model) has thus been selected for its advantageous mesh size.

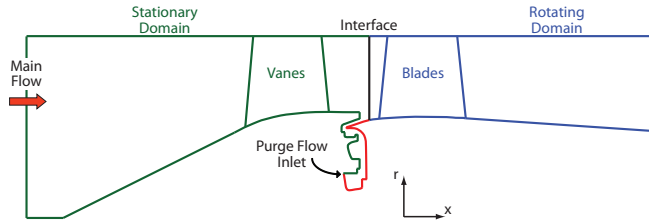


FIGURE 2. Configuration B : side view of the computational domain. Green color represents the stationary domain while blue color shows the rotating one. Red colored lines represent the rotating wall in the stationary domain. Shroud radius is 0.329 m and cavity minimum radius is 0.262 m.

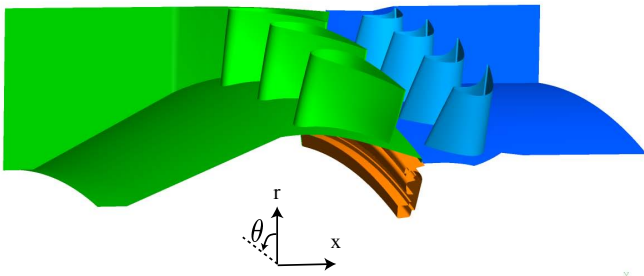


FIGURE 3. 3-D domain - Configuration B.

For configuration A, computations carried out on a full 360° domain showed similar flow physics as on the selected 180° sector. This simplified geometry is meshed using hexahedral elements with an azimuthal resolution of $1^\circ/\text{cell}$, for a total number of 500 000 cells. Finer circumferential resolutions were also tested without significant changes in CO_2 and temperature fields. The aspect ratio of the cells near the wall remains smaller than 10 and minimum face angle is 15° . For the second configuration (B), a mixed element (hex, tet) mesh is employed and the circumferential resolution is set at $0.5^\circ/\text{cell}$. Following the procedure proposed in Julien *et al.* [11], the no-slip condition is used for the resolution of boundary layers on the hub and the cavity walls while slip conditions are imposed on the vanes, blades and shroud, allowing an important cell count reduction without affecting ingestion and cooling effectiveness diagnoses. The resulting number of elements for configuration B is 510 000. The aspect ratio of the cells adjacent to the cavity walls is around 5. Again, a finer circumferential resolution was tested ($0.25^\circ/\text{cell}$) without affecting the resulting conclusions of the study.

For both configurations, periodicity conditions are imposed in the circumferential direction. High resolution schemes implemented in ANSYS CFX were used for turbulence numerics

and advection. A second order backward euler scheme was employed for the transient term. Simulations were run long enough to reach satisfactory statistical convergence, that is when the time averages of monitored quantities in the cavity (temperature or CO_2 concentration) remain invariant with respect to longer time averaging periods (typically, one revolution period). The last revolution is run at 600 timesteps/cycle for configuration A and at 2900 timesteps/cycle (50 timesteps/blade pass and RMS Courant number near 1) for configuration B. The *RET* runs typically took a longer time than *ILT* runs to stabilize and reach statistical convergence. The criterion for iterations convergence (RMS) is $1e-6$ for all quantities and was attained in about 10 iterations per timestep for the last revolution. A complete simulation (case) took from 50 to 80 hours on 24 Intel Nehalem processors (6 quad cores) with Infiniband connexions.

Similarity and Flow Conditions

As mentioned before, test rig conditions characterized by isothermal low temperature ($T = 300$ K) and low pressure conditions are referred to as *ILT*. Gaspath and purge inlets are both at the same temperature, while CO_2 concentration ψ is set to 1 at the purge flow entrance and 0 at the gaspath inlet. On the other hand, the temperature condition at gaspath inlet for a typical real engine case (referred to as *RET*) is set at $T_{\text{gaspath}} = 1800$ K. In order to preserve velocity triangles between the two scenarios of conditions, standard turbomachinery similarity parameters were used with the *ILT* conditions as analysis basis. Since geometries are the same (identical gaspath radii for both cases), Mach numbers are low and the same gas is used, there are two parameters (which are dimensional) that need to be respected to fully define similar operating points of the turbine : Ω/\sqrt{T} and $\dot{m}_{\text{gaspath}}\sqrt{T}/P_{\text{gaspath}}$.

Table 1 shows the respected parameters with *ILT* conditions being set as a basis and *RET* conditions being determined to satisfy similarity. Additionally, since the flow rate requirement for typical rigs is approximately half of real engine flow, *RET* gaspath mass flow is imposed at 6 kg/s. Due to differences in viscosity and density values between the two scenarios, rotational Reynolds number similarity is not enforced. However, this is not expected to play a significant role in assessing the validity of the CO_2 tracer use.

For each simulation, the gaspath inlet boundary condition is set as an axisymmetric total pressure (P_0) while the outlet (\dot{m}_{outlet}) and the purge inflow (\dot{m}_{purge}) are based on mass flow conditions. Since no blades and no vanes are used in the simple configuration (A), cylindrical components are imposed at the gaspath inlet to be representative of the flow orientation at that location in a real engine.

TABLE 1. Boundary conditions and similarity parameters used for both scenarios : Isothermal Low Temperature (ILT) and Real Engine Temperature (RET). Standard SI units are used.

	ILT	RET
$\Omega/\sqrt{T}(s^{-1}K^{-0.5})$	14.43	
$\dot{m}_{\text{gaspath}}\sqrt{T}/P_0$	4.25E-04	
T_{gaspath} (K)	300	1800
Ω (rad/s)	250	612
\dot{m}_{gaspath} (kg/s)	2.7	6.0
$P_{0,\text{inlet}}$ (Pa)	110 000	600 000
Re_ϕ	1 342 000	168 160

Three purge flow rates, $\Phi_{\text{purge}} = 0.05\%$, 0.25% and 0.50% (which correspond to $C_{w,\text{ILT}} = 244$, 1220 and 2440 and $C_{w,\text{RET}} = 60$, 300 and 600 respectively) are considered. Note here that C_w values differ for *ILT* and *RET* cases due to the dependance of viscosity with temperature. The chosen similarity parameter enforced for purge mass flow is $\Phi_{\text{purge}} (\dot{m}_{\text{purge}} / \dot{m}_{\text{gaspath}})$ in order to link gaspath and purge dynamic conditions. Purge flow enters the cavity with a circumferential velocity of half that of the rotor ($\Omega R/2$) and its orientation is thus variable depending on the mass flow rate imposed.

The CO_2 molecular diffusivity coefficient D_Ψ is set to a constant value of $1.6E-05 \text{ m}^2/\text{s}$ for *ILT* cases. For *RET* cases, despite the expected importance of turbulent diffusion over molecular diffusion, the CO_2 diffusivity (D_Ψ) is defined as a function of temperature and pressure using a non-isothermal correlation [17]:

$$D_\Psi = 1.6E-05 \left(\frac{T}{300K} \right)^{3/2} \left(\frac{P}{101300Pa} \right)^{-1} \text{ m}^2/\text{s}.$$

This had only minor effects on the observed fields but the use of the variable coefficient was nonetheless kept for all *RET* simulations to remain rigorous.

4 RESULTS

Numerical results are divided as follows. The correlation between the CO_2 and the thermal fields in the context of real engine temperature conditions is first presented. Comparisons between sealing efficiency predictions from *ILT* and *RET* simulations are then addressed. Unsteadiness issues, geometrical effects and general results for both configurations are discussed.

Config. A is used as a preliminary case to illustrate seal design effects and rotationally-induced ingress while Config. B is used to demonstrate the influence of vanes and blades as well as the effectiveness of a better rim seal design on ingestion.

For the purpose of visualization, scalar fields will be shown on $r - \theta$ planes with an axial positioning near the middle of the cavity. Their approximate positions are shown in Fig. 4. Bounded planes where scalar quantities are averaged radially at each constant θ position are called “clip planes” and are also used for ingress diagnoses comparisons as they indicate radially-averaged quantities associated to particular plane positions. These $r - \theta$ bounded planes are shown in Fig. 4. Numbered monitor points 1 and 2 used for configuration B are also indicated in the figure.

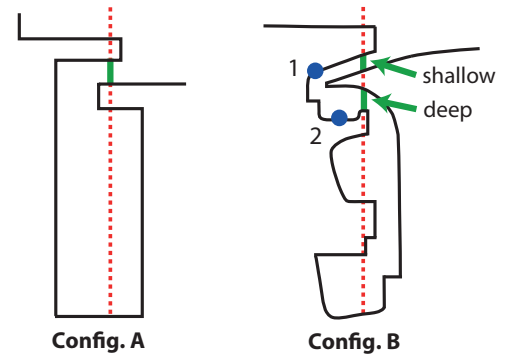


FIGURE 4. Axial positioning of the visualization planes (red) and clip planes (green) used for circumferential ingress analysis in configurations A & B. Monitor points as well as two different clip planes (“shallow plane” and “deep plane”) are used for configuration B analysis.

Normalized CO_2 and thermal fields will be used and are defined respectively as :

$$\eta_{CO_2} = \frac{\Psi - \Psi_{\text{gaspath}}}{\Psi_{\text{purge}} - \Psi_{\text{gaspath}}}, \quad \eta_{\text{thermal}} = \frac{T_{\text{gaspath}} - T}{T_{\text{gaspath}} - T_{\text{purge}}}.$$

A value of 1 indicates no trace of gaspath properties which represents perfect sealing, while a value of 0 indicates full gaspath properties (either temperature or concentration) and thus, no sealing at all. Values of η are locally averaged in r on clip planes to obtain a circumferential θ distribution, which can be specified as :

$$\eta_\theta \equiv \eta(\theta) = \int \eta(r, \theta) dr$$

and global averaging over the entire plane is also performed.

It is important to keep in mind that the value of sealing effectiveness highly depends on the choice of the clip planes, and therefore comparing η values from one configuration to another may be ambiguous. However, using those planes to compare different operating conditions on a given configuration is rigorous and adequate. In the context of rim seal designed to prevent hot gas ingestion, one is formally concerned with η_{thermal} and wishes that η_{CO_2} provides a reasonable approximation of the former. This question is addressed here, first when both diagnoses are computed under the same real engine temperature conditions, and then, when η_{CO_2} is computed under cold rig condition.

4.1 Passive Scalar Predictions in Real Engine Temperature Settings

Before addressing the question as to whether cold rig experiments can yield representative and useful results with regards to sealing effectiveness in real engine temperature ranges, one must first confront η_{CO_2} and η_{thermal} results within a same *RET* computation. In other words, one has to assess first the similarity of these fields before proceeding next to the comparison of η_{CO_2} in isothermal low temperature condition versus η_{thermal} for real engine temperature cases.

Figure 5 illustrates sealing effectiveness contours based on the thermal and CO_2 fields for computations performed on configuration A with $\Phi_{\text{purge}} = 0.25\%$ (*RET*). Both fields present moderate ingestion of main gaspath flow (low η values) and are in excellent agreement, although the CO_2 field yields a slightly better mean sealing than the thermal field. Evaluation of the circumferential evolution (η_{θ}) at the clip plane (Fig. 6) shows quasi-periodic oscillations of η_{CO_2} and η_{thermal} . Both figures demonstrate zones of high temperature (hot spots) and of high concentration with the same trends in amplitude and number. The η_{thermal} signal amplitude is slightly lower due to higher temperatures created by the rotating disk (additional viscous work term) which has no equivalent in the CO_2 equation. Average values are 0.269 and 0.256 for η_{CO_2} and η_{thermal} respectively.

Similar agreement (not shown) is observed in configuration A for other purge flow rates ($\Phi_{\text{purge}} = 0.05\%$ and 0.50%) as well as for configuration B. It is therefore accepted that, for real engine thermal conditions, sealing effectiveness predicted by means of a passive CO_2 tracer is representative of that based on temperature.

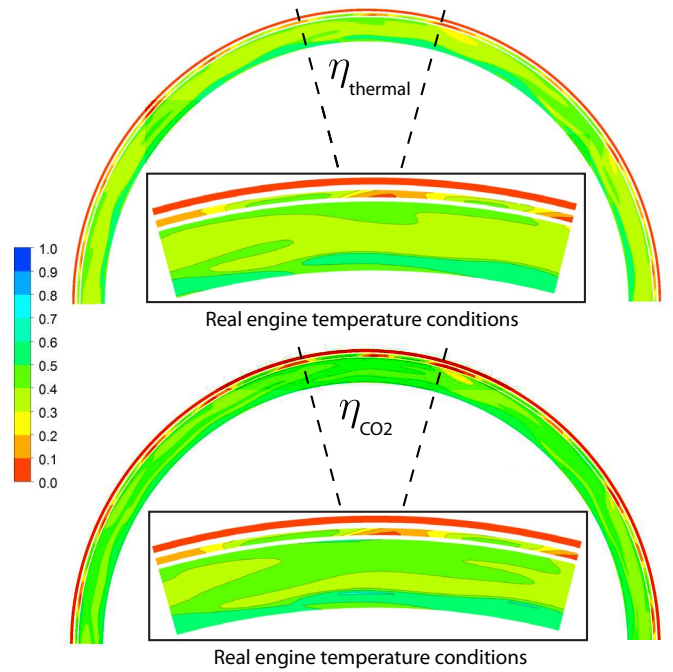


FIGURE 5. Configuration A - $\Phi_{\text{purge}} = 0.25\%$, *RET*, mid-cavity η_{CO_2} and η_{thermal} instantaneous fields at final time (shown on complete 180° geometry and 30° sector zoom.)

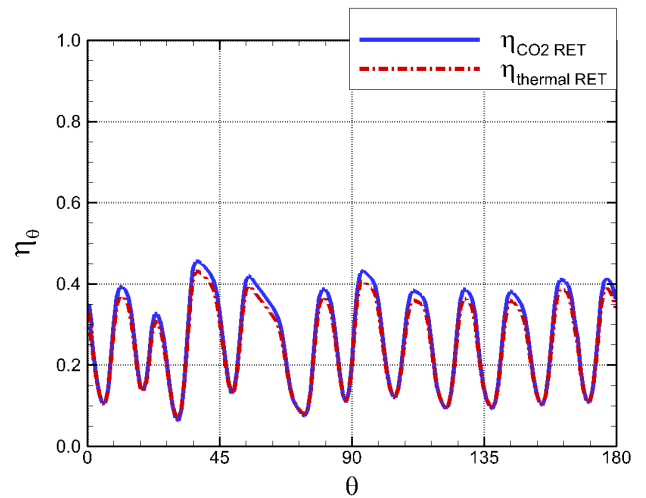


FIGURE 6. Configuration A - $\Phi_{\text{purge}} = 0.25\%$, *RET* - η_{CO_2} and η_{thermal} circumferential signals for the instantaneous fields at final time.

4.2 Simplified Geometry - Configuration A

Main results for configuration A are presented here. Two cases are considered, a very low purge flow rate ($\Phi_{\text{purge}} = 0.05\%$) and a typical purge flow rate ($\Phi_{\text{purge}} = 0.50\%$). For each case, isothermal low temperature condition is compared to its real engine settings counterpart.

Instantaneous results at final time for the very low purge flow case are shown in Figs. 7 (on a 30° sector for visualization purposes) and 8. A minimal amount of purge flow is provided to the cavity, resulting in low values of sealing effectiveness from both predictors. Quasi-periodic fluctuations are viewed through clip plane analysis (see Fig. 8) and the same number of structures is observed. These are generated even though gaspath and purge flows are axisymmetric. A good agreement is observed but sealing effectiveness from the temperature field for *RET* slightly overestimates η_{CO_2} , as can be seen on Fig. 7, and a similar observation is also noted from the global averaging of the sealing effectiveness at the clip planes which gives $\eta_{CO_2} = 0.053$ and $\eta_{thermal} = 0.063$ at that location. Discrepancies are very small considering the fact that these simulations are run under significantly different dimensional flow conditions, but nonetheless analogous as far as similarity conditions are concerned.

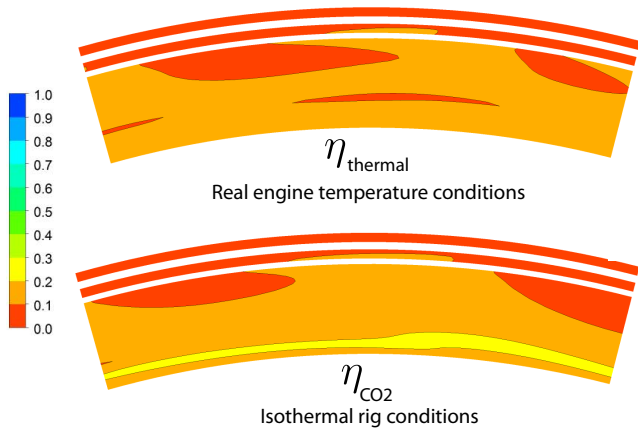


FIGURE 7. Configuration A - $\Phi_{purge} = 0.05\%$ - 30° visualization sectors of mid-cavity η_{CO_2} and $\eta_{thermal}$ instantaneous fields at final time.

On the other hand, comparison of sealing effectiveness contours for the typical purge flow case ($\Phi_{purge} = 0.50\%$) shows that passive tracer values at *ILT* overestimate cooling effectiveness at *RET* (see Fig. 9). The relative differences are more important here than for the low purge flow case. Indeed, signals at the clip plane (Fig. 10) indicate regular oscillations along θ of high amplitude (± 0.20 in η) with a global averaging of 0.499 for η_{CO_2} and 0.442 for $\eta_{thermal}$. This time, the number of circumferential structures associated to temperature or concentration peaks differs for both predictors. The structure count is here higher in the cold rig versus the real engine temperature conditions case (14 and 12 respectively in the 180° sector). At this point, it thus appears that the large flow structures play a key role on the three-dimensionality of the ingestion process, and that their circumferential count seems affected by the thermal conditions.

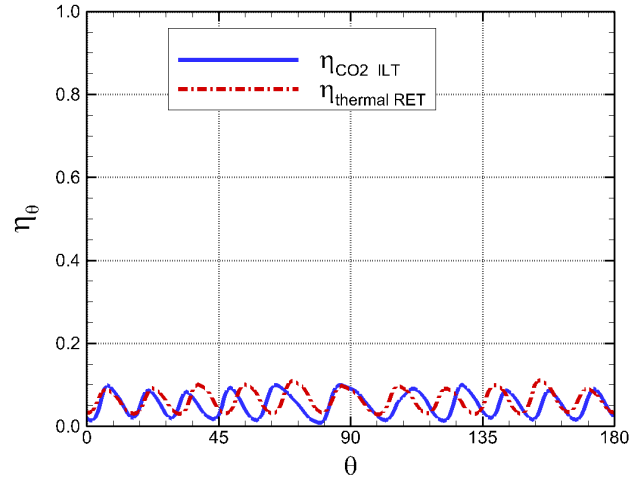


FIGURE 8. Configuration A - $\Phi_{purge} = 0.05\%$ - η_{CO_2} and $\eta_{thermal}$ circumferential signals for the instantaneous fields at final time.

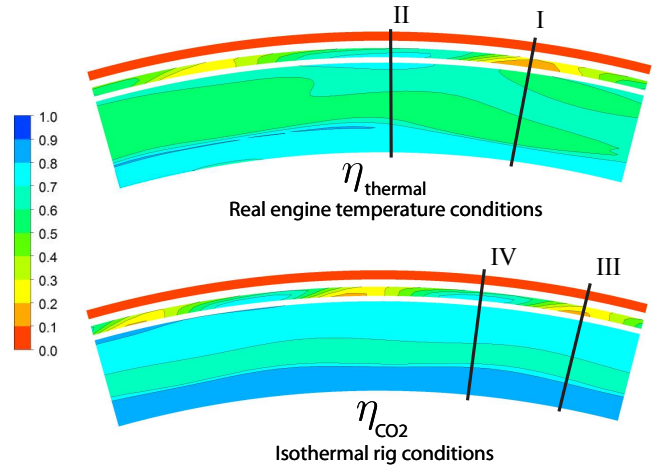


FIGURE 9. Configuration A - $\Phi_{purge} = 0.50\%$ - 30° visualization sectors of mid-cavity η_{CO_2} and $\eta_{thermal}$ instantaneous fields at final time.

Nonetheless, we observe similar signal amplitudes and mean values between η_{CO_2} and $\eta_{thermal}$ in both Fig. 8 and Fig. 10 once again despite the fact that running conditions differ largely between both types of simulations.

For the typical purge flow case ($\Phi_{purge} = 0.50\%$), the ingestion phenomenon is now visualized on planes representing either ingress (Planes I and III) or egress (Planes II and IV). Figure 11 shows a display of tangential velocity vectors as well as the sealing efficiency on $r-x$ planes at specific θ locations. Occurrence of ingress is characterised by inward velocity vectors and lower efficiency at the seal whereas egress shows outward flow and higher values of η at that location. Overall flow behaviors based on tangential velocity vectors and temperature or CO_2 tracer fields are fairly similar.

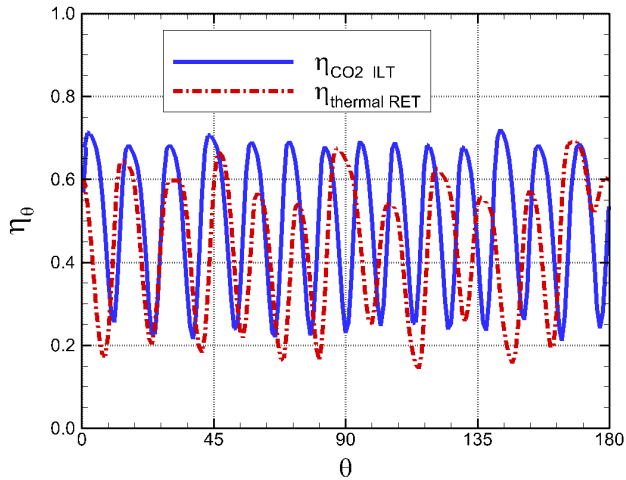


FIGURE 10. Configuration A - $\Phi_{\text{purge}} = 0.50\%$ - η_{CO_2} and η_{thermal} circumferential signals for the instantaneous fields at final time.

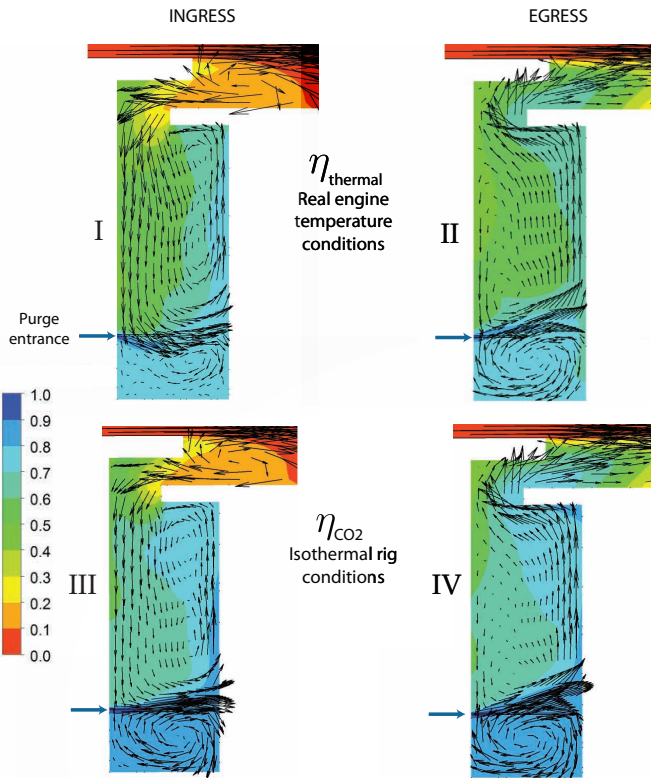


FIGURE 11. Instantaneous tangential velocity vectors and sealing efficiency fields showing ingress (Planes I and III) or egress (Planes II and IV) for Configuration A - $\Phi_{\text{purge}} = 0.50\%$. Station locations refer to the planes identified in Fig. 9.

Note that the same mass flow proportion (% of gaspath flow) is set at the purge flow inlet for the *ILT* and *RET* cases, but imposed temperature and local pressure yield a purge flow density about three times lower for the low temperature conditions. As a result, even if a higher mass flow is set at the purge entrance of the *RET* case, axial velocities are slightly higher for the *ILT* cases, as shown in Fig. 11. Tangential velocities are however more important in the *RET* case due to higher rotation speed.

4.3 Real Engine Geometry - Configuration B

Simulations performed on configuration B are now presented in order to assess the behavior of the passive tracer in a more realistic engine geometry with vanes and blades. Figures 12 and 13 show time monitoring (points shown on Fig. 4) of the last half revolution and associated spectral analysis (on the whole last revolution) of the η_{CO_2} and η_{thermal} fields for the $\Phi_{\text{purge}} = 0.25\%$ case. In the spectral signals, the abscissa f^* represents occurrences per engine revolution. On the considered monitor points, it can be seen that the influence of blade passage ($f^* = 58$) is less important than expected. A far more energetic frequency ($f^* \approx 23$) corresponding to the effect of large-scale structure passages is observed and seems to have a similar influence on the η_{CO_2} signal in the cold rig case and the η_{thermal} in the real engine case. Fluctuations in η are more severe for the *ILT* case but structure count is the same.

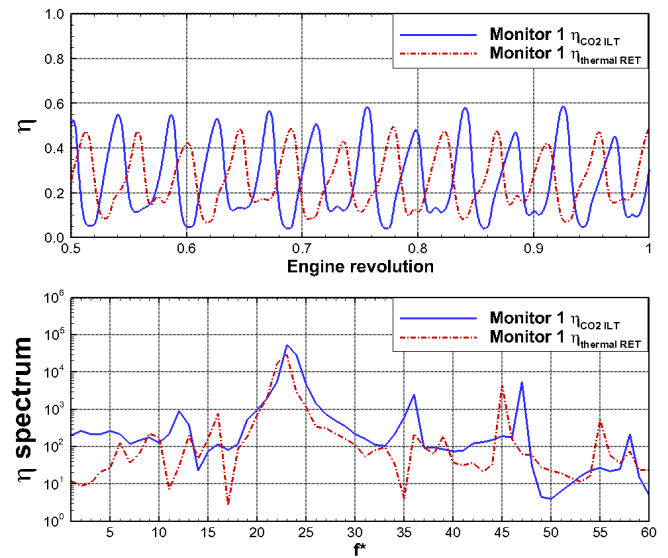


FIGURE 12. η_{CO_2} in *ILT* conditions versus η_{thermal} in *RET* conditions: time signals for monitoring point 1 (see Fig. 4) on the cavity stationary wall of configuration B - $\Phi_{\text{purge}} = 0.25\%$.

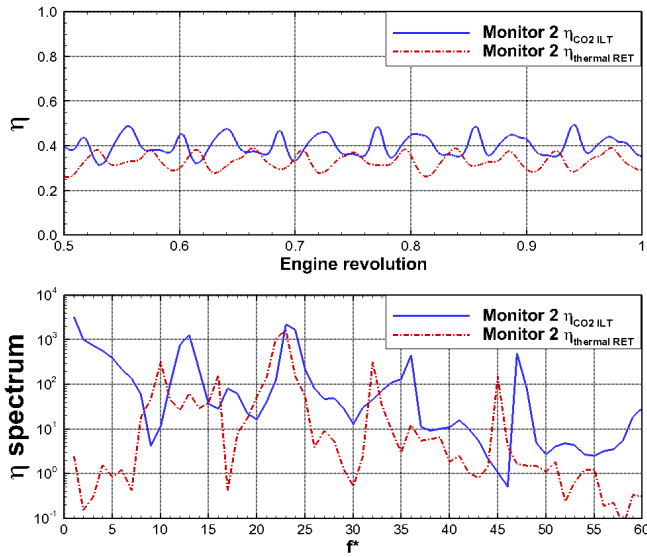


FIGURE 13. η_{CO_2} in ILT conditions versus $\eta_{thermal}$ in RET conditions: time signals for monitoring point 2 (see Fig. 4) on the cavity stationary wall of configuration B - $\Phi_{purge} = 0.25\%$.

For the same case, spatial distribution of these structures is now examined. Figure 14 first shows the circumferential pressure distribution on the upper wall of the cavity and rotor hub, which acts as an overall boundary condition for the problem. Note that even if pressure levels are not exactly identical, fluctuations share a common order of magnitude ($\approx 1\% P_0$). Figure 15 then shows the instantaneous cavity sealing efficiency fields on the upper rotor wall of the 3 vanes - 4 blades sector ($\approx 24^\circ$) for the $\Phi_{purge} = 0.25\%$ case. Two $r-x$ planes are also shown at different circumferential locations. These fields are characterized by the presence of two large-scale flow structures causing temperature and CO_2 concentration gradients, which are also noticed on both deep and shallow planes analysis η_θ shown in Fig. 16. Global average values at those locations are $\eta_{CO_2} = 0.775$ and $\eta_{thermal} = 0.697$ (deep), and $\eta_{CO_2} = 0.235$ and $\eta_{thermal} = 0.250$ (shallow). These two structures would result in 29 regions of high and low pressure resulting in 29 hot spots or high concentration zone on a full 360° geometry. Their angular velocity is determined by combining the spatial and temporal information. By dividing f^* (23) by the total number of structures on the 360° geometry (29), it is found that these structures rotate at about 79% of the rotor speed for both cases compared.

Again, the cold rig sealing effectiveness predicted by the computed CO_2 values show fairly good agreement with the sealing RET values based on the temperature field. At the deep ingress plane, CO_2 predictions slightly overestimate maximum thermal ingestion, as was observed in Configuration A. When

comparing both η_{CO_2} and $\eta_{thermal}$ at the shallow ingress plane in Fig. 16, one observes that maximum values are higher for the CO_2 field. However, the global average values are slightly higher for the thermal field compared to the CO_2 predictor in this case. This suggests that the large scale flow structures present in both scenarios, and associated with the observed circumferential variations in η , are not quite identical in size and in strength, but rotate at a similar angular speed. Thermal conditions thus appear to affect such aspects of the the flow topology and dynamics.

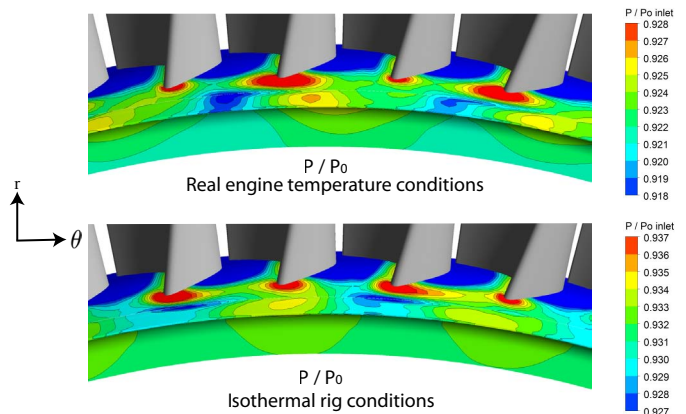


FIGURE 14. Configuration B - $\Phi_{purge} = 0.25\%$, $r-\theta$ view of instantaneous pressure fields at final time. Both color scales span $1\% P_0$.

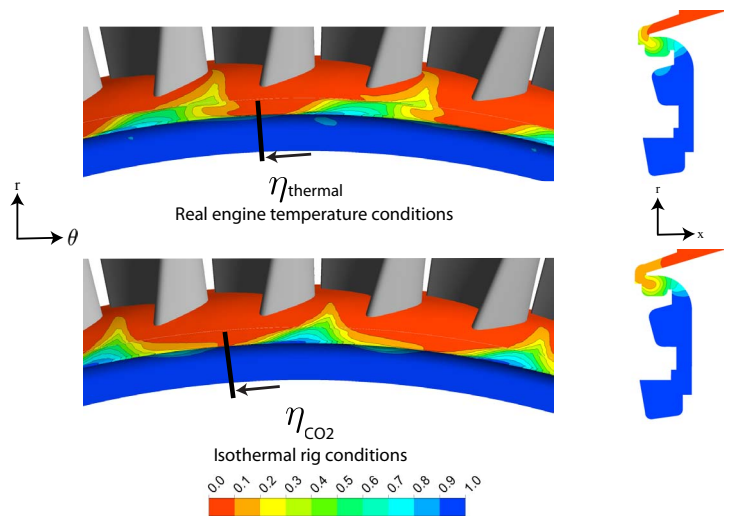


FIGURE 15. Configuration B - $\Phi_{purge} = 0.25\%$, $r-\theta$ and $r-x$ views of η_{CO_2} and $\eta_{thermal}$ instantaneous fields at final time. Chosen $r-x$ view planes on the right are located (circumferentially) where maximum ingress is observed for each case.

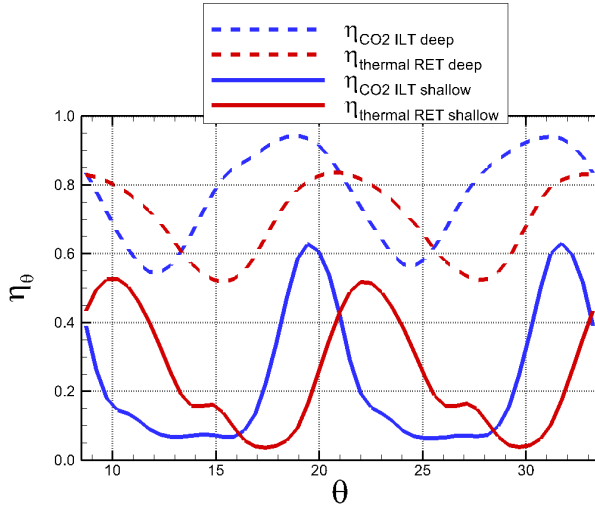


FIGURE 16. Configuration B - $\Phi_{\text{purge}} = 0.25\%$ - η_{CO_2} and η_{thermal} circumferential signals on a shallow and deep plane (see Fig. 4 for exact positioning).

Finally, the $\Phi_{\text{purge}} = 0.05$ and 0.50% cases show similar behaviors in both temporal and spatial signals. It was noted however that better sealing effectiveness predictions are made for cases with larger purge flow rates.

5 CONCLUSION

Unsteady simulations of turbine disk cavity and gaspath flows were performed in order to investigate the validity of using a passive scalar marker to model thermal ingestion through the rim seal region. In this first phase of the investigation, we have restricted our study to conditions remaining in a low subsonic regime. Similarity parameters were established and used to make this comparison between real engine and rig type simulations fair and adequate. A simplified geometry and a 24° turbine stage sector with vanes and blades have been used to determine if thermal ingress related phenomena found in real engine settings can be captured similarly by a CO_2 field in a cold rig environment.

First, it has been verified that the passive marker can model the thermal field adequately when it is used in real engine temperature conditions. With all the tests performed, we have found that η_{CO_2} and η_{thermal} scalar fields in a same real engine simulation behave in a similar way.

Second and most importantly, comparisons between the η_{thermal} field in real engine temperature settings and the η_{CO_2} field in an isothermal (cold rig) case were made. It was found that the cold rig predictor tends to slightly overestimate the

local sealing effectiveness, while providing the right trends and reasonably accurate mean levels of actual sealing. Three-dimensional flow structures known to affect ingestion appear to be sensitive to the thermal and operating conditions. Their circumferential number and strength differed slightly between the two scenarios of conditions but their angular speed was similar.

At this stage of the investigation, it thus seems appropriate to use passive tracer in cold rig experiments to compare performances of different rim seal designs. However, it would seem risky to predict a quantitative value of sealing effectiveness under real engine operating conditions from the CO_2 tracer in a cold rig.

The next phase of the investigation will include tests with different purge flow similarity conditions and wall heat conduction in order to push the comparison towards more complete and realistic engine conditions. We also intend to better identify the origin of the large-scale structures observed in the lip seal region, and their relationship with cavity flow physics.

ACKNOWLEDGMENT

Financial support from CRIAQ and Ministère du Développement Économique du Québec (MDEIE-PSR-SIIRI-144) as well as computing time provided by the CLUMEQ supercomputer consortium is gratefully acknowledged by the authors.

REFERENCES

- [1] Owen, J.M., and Rogers, R.H., 1989. "Flow and Heat Transfer in Rotating-Disc Systems - Vol.1 - Rotor-Stator Systems". *John Wiley and Sons Inc.* New York.
- [2] Phadke, U.P., and Owen, J.M., 1988. "Aerodynamic Aspects of the Sealing of Gas Turbine Rotor-Stator Systems, part 2 : The behavior of simple shrouded rotating-disk systems in a quiescent environment". *Int. J. of Heat and Fluid Flow*, Vol.9, No.2.
- [3] Phadke, U.P., and Owen, J.M., 1988. "Aerodynamic Aspects of the Sealing of Gas Turbine Rotor-Stator Systems, part 1 : The performance of simple seals in a quasi-axisymmetric external flow". *Int. J. of Heat and Fluid Flow*, Vol.9, No.2.
- [4] Chew, J.W., Dadkhah, S., and Turner, A.B., 1992. "Rim Sealing of Rotor-Stator Wheelspaces in the Absence of External Flow". *ASME Journal of Turbomachinery*, **114** (433-438).

- [5] Chew, J.W., Green, T., and Turner, A.B., 1994. "Rim Sealing of Rotor-Stator Wheelspaces in the Presence of External Flow". ASME Paper 94-GT-126.
- [6] Bayley, F.J., and Childs, P.R.N., 1997. "Prediction of Ingress Rates to Turbine and Compressor Wheelspaces". *Int. J. Heat and Fluid Flow*, vol.18:218-228.
- [7] Hills, N.J., Chew, J.W., and Turner, A.B., 2002. "Computational and Mathematical Modeling of Turbine Rim Seal Ingestion". *J. of Turbomachinery*, **124**(2), April, pp.306-315.
- [8] Gentilhomme, O., Hills, N.J., Turner, A.B., and Chew, J.W., 2003. "Measurements and Analysis of Ingestion Through a Turbine Rim Seal". *J. of Turbomachinery*, **125**(3), July, pp. 505-512.
- [9] Roy, R.P., Zhou, D.W., Ganesan, S., Wang, C.-Z., Paolillo, R.E., and Johnson, B.V., 2007. "The Flow Field and Main Gas Ingestion in a Rotor-Stator Cavity". ASME Paper GT2007-27671.
- [10] Chew, J.W., 2009. "Developments in Turbomachinery Internal Air Systems". *Proc. IMechE Part C: J. Mechanical Engineering Science*, **223**(1), pp. 189-234.
- [11] Julien, S., Lefrancois, J., Dumas, G., Boutet-Blais, G., La-pointe, S., Caron, J.-F., and Marini, R., 2010. "Simulations of Flow Ingestion and Related Structures in a Turbine Disk Cavity", ASME Paper GT2010-22729.
- [12] Jakoby, R., Zierer, T., Lindblad, K., Larsson, J., deVito, L., Bohn, D.E., Funcke, J., and Decker, A., 2004. "Numerical Simulation of the Unsteady Flow Field in an Axial Gas Turbine Rim Seal Configuration", ASME Paper GT2004-53829.
- [13] Cao, C., Chew, J.W., Millington, P.R., and Hogg, S.I., 2004. "Interaction of Rim Seal and Annulus Flow in an Axial Flow Turbine". *J. of Eng. for Gas Turbines and Power*, **126**(4), October, pp.786-793.
- [14] Boudet, J., Autef, V.N.D., Chew, J.W., Hills, N.J., and Gentilhomme, O., 2005. "Numerical Simulation of Rim Seal Flows in Axial Turbines". *Aeronautical Journal*, **109**(1098), August, pp.373-383.
- [15] ANSYS CFX, 2009. *User's Guide*. ANSYS CFX-Solver, Release 12.0.
- [16] Feiereisen, J.M., Paolillo, R.E., and Wagner, J., 2000. "UTRC Turbine Rim Seal Ingestion and Platform Cooling Experiments". AIAA Paper 2000-3371.
- [17] Incropera, F.P., Dewitt, D.P., Bergman, T.L., and Lavine, A.S., 2006. "Fundamentals of Heat and Mass Transfer". *John Wiley and Sons Inc.* 6th edition. New York. p. 952.